Power Electronic Systems
Laboratory

Proceedings of the 28th Applied Power Electronics Conference and Exposition (APEC 2013), Long Beach, California, USA, March 17-21, 2013

Analysis of Rotary Transformer Concepts for High-Speed Applications

D. Bortis,
L. Fässler,
A. Looser,
J. W. Kolar

Eidgenössische Technische Hochschule Zürich
Swiss Federal Institute of Technology Zurich

Analysis of Rotary Transformer Concepts for High-Speed Applications

Dominik Bortis, Lukas Fässler, Andreas Looser and Johann W. Kolar
Power Electronic Systems Laboratory
ETH Zurich
Physikstrasse 3, 8092 Zurich, Switzerland
Email: bortis@lem.ee.ethz.ch

***Abstract*—In many applications electrical energy has to be transferred to rotating parts. Usually a cylindrical transformer with a rotating and a stationary part is used, which are separated by a small air gap. In order to achieve a high magnetic coupling, on both parts a highly permeable core material is employed. In high-speed applications the diameter of the rotary transformer should be small since the mechanical stresses can be high. Therefore, a high electrical frequency has to be selected. This high switching frequency would result in high core losses; ferrite would be the best suited material. However, ferrite is brittle and has a limited mechanical strength. Therefore, in this paper two concepts of rotary transformers are analyzed, where no core material is used on the rotating part. The major advantage of these concepts is a simple and mechanically robust design with a lightweight construction resulting in very small unbalanced mass.**

I. Introduction

In grinding processes of hard ceramics, usually spindles with rotational speeds of up to 100'000 rpm are used. There, the processing time and the cost of the diamond equipped grinding tools are high. In order to reduce the processing time and the abrasion of the expensive tools, new approaches are investigated, where, in addition to the rotation of the grinding tool, an axial ultrasonic vibration is superimposed [1]–[3]. The generation of the ultrasonic vibration is realized with a piezo-electric resonator attached to the rotating part of the spindle, whereby the electrical energy is supplied from the stationary part.

The electrical energy transfer to the rotating part is usually realized with a rotary transformer, where most concepts presented in the literature [4]–[8] are based on the two structures shown in Fig. 1 a) and b), where depending on the mechanical arrangement the air gap is either radial or axial. With the magnetic core material employed on the rotating and stationary parts, and the small air gap, a high

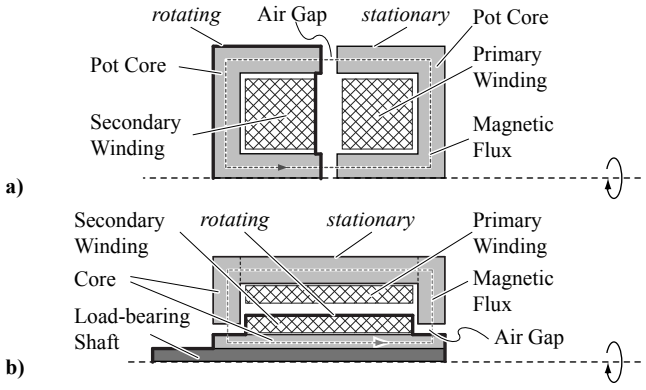

Fig. 1. Cross section of the basic rotary transformer concepts with a) axial and b) radial air gap.

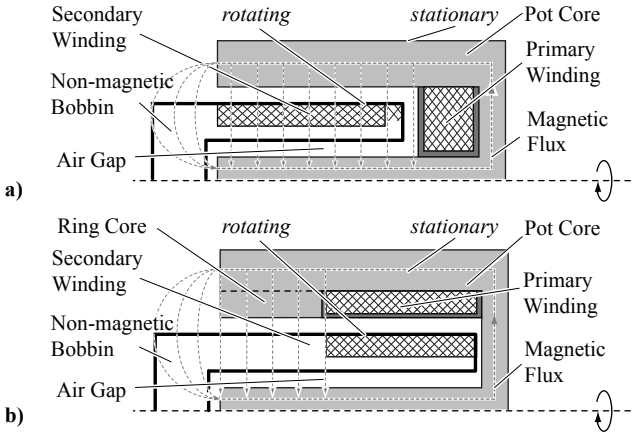

Fig. 2. Cross section of analyzed rotary transformer concepts without magnetic material on the rotating part. a) concept 1: secondary winding arranged in the air gap. b) concept 2: secondary fully enclosed by the major part of the magnetic flux.

magnetic coupling is achieved, which is the major advantage of these concepts. In high-speed applications, however, due to the high mechanical stresses, the diameter of the rotary transformer has to be minimized, which on the one hand results in a long transformer with a small core cross section. On the other hand, to down-size the overall dimensions of the transformer a high electrical frequency has to be selected, which demands suited magnetic materials to keep the core losses low. Sintered ferrite-cores, however, are brittle and show only a low mechanical strength. In addition, compared to the windings, the core material's mass is high, which leads to a high unbalanced mass in the rotating part.

To overcome these limitations, two rotary transformer concepts for high-speed applications (one concept was basically proposed in [9]) are analyzed and compared in this paper, where no magnetic material is employed on the rotating part. These concepts feature a simple and mechanically robust design with a lightweight construction resulting in very small unbalanced mass, which is presented in Section II. Based on the derived reluctance model, in Section III, the magnetic and electrical performances are evaluated for both concepts. There, also the mechanical stabilities are analyzed. An experimental comparison of both concepts with prototypes for an output power of 200 W, an electrical frequency of 70 kHz, and a rotational speed of 60'000 rpm is finally done in Section VI.

II. Description Of Rotary Transformer Concepts

In Fig. 2 the cross sections of the analyzed rotary transformer concepts for high speed applications are shown. The rotating part consists of a strong non-magnetic bobbin, e.g. based on PEEK. It is

designed as a hollow cylinder with thin walls carrying the secondary winding and is extended into the stationary pot core. The primary winding - wound on a plastic bobbin - is also placed inside the pot core and either arranged next to (concept 1, Fig. 2 a)) or around (concept 2, Fig. 2 b)) the secondary winding. Depending on these winding arrangements, different magnetic couplings are achieved. However, due to mechanical stability reasons, for both concepts, the rotor's walls are limited to a certain minimum thickness, thus resulting in a relatively large air gap $h_{\mathrm{air,tot}}$ (cf. Fig. 3 a)) and low magnetic coupling compared to the basic concepts shown in Fig. 1. In order to improve the magnetic coupling, for concept 2 a ring core is placed next to the primary winding. Thus, the air gap width is mainly defined by the ring core width l_{a} (cf. Fig. 8 a)) and all turns of the secondary winding are linked with the major part of the magnetic flux. However, due to the additional ring core the rotor is elongated which can result in a worse mechanical stability.

For concept 1 the air gap is distributed over the whole length of the secondary winding l_{w2}, which is in general larger than l_{a} and would lead to a better coupling. However, since in concept 1 also the magnetic flux is evenly distributed over the whole length l_{c} - assuming an ideal core material - not all turns of the secondary winding are fully linked with the primary's magnetic flux; accordingly, the magnetic coupling is again reduced. On the other hand, the rotor length can be kept small resulting in improved rotor dynamics. Therefore, to compare these two concepts, a detailed magnetic, electrical and mechanical analysis is performed in the following.

III. Transformer Design

A. Magnetic Design

In order to describe the magnetic behavior of the rotary transformer concepts, first, the magnetic field distribution in the air gap has to be derived. Due to the rotationally symmetric design, cylindrical coordinates (r, z, φ) can be used for the magnetic field, whereas due to symmetry reasons for both rotary transformer concepts the magnetic field H has no φ-component ($H_{\varphi} = 0$).

In Fig. 3 a) the cross section of concept 1, the qualitative distribution of the magnetic fields $H_{\mathrm{r},1}$ and $H_{\mathrm{r},2}$ of the primary and

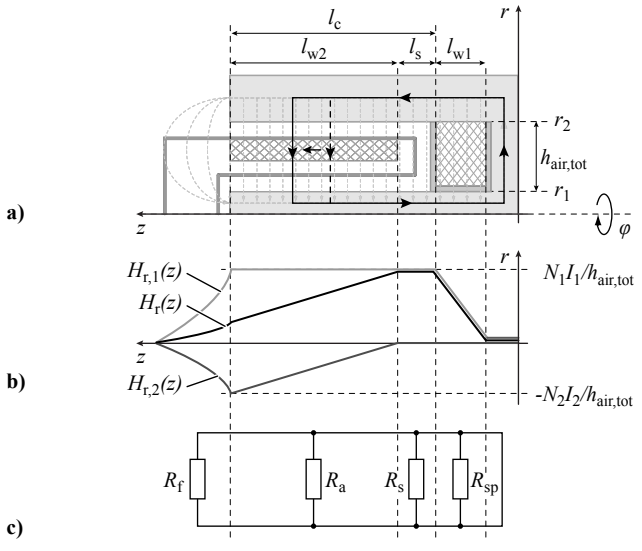

Fig. 3. Cross section of the rotary transformer (drawing not to scale), schematic H-field distribution $H_{\mathrm{r}}(z)$ and mag. reluctances for concept 1.

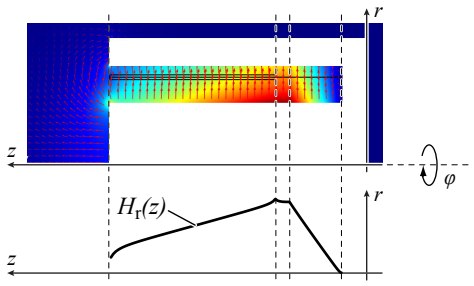

Fig. 4. FEM-Simulation of the magnetic field $H_{\mathrm{r}}(z)$ for concept 1.

secondary winding respectively, and the resulting magnetic field H_{r} (found by superposition of $H_{\mathrm{r},1}$ and $H_{\mathrm{r},2}$) are shown. Inside the core window over the length l_{c}, the magnitude of the magnetic fields $H_{\mathrm{r},1}$ and $H_{\mathrm{r},2}$ - assuming an ideal core material ($\mu_{\mathrm{r}} \to \infty$) - can be found by Ampère's law with a rectangular closed loop path, whereas the loop path's width is continuously enlarged in z-direction as illustrated in Fig. 3 a). With the number of turns enclosed by the loop path, the current value and the air gap length within the loop path, the magnetic field's magnitude in radial direction can be calculated, if it is assumed that the radial component of the magnetic-field is constant; this is a good approximation as long as $r_1 \gg (r_2 - r_1)$ (drawing not to scale). Thus, inside the primary winding the magnitude of $H_{\mathrm{r},1}$ is linearly increasing to approximately $N_1 I_1 / h_{\mathrm{air,tot}}$ and stays constant inside the core window over the length l_{c}. On the other hand, the magnitude of $H_{\mathrm{r},2}$ is zero over the length l_{w1} and l_{s} - no secondary current is enclosed - and decreases linearly along the z-axis inside the secondary winding to approx. $-N_2 I_2 / h_{\mathrm{air,tot}}$ when all secondary turns are enclosed (cf. Fig. 3 a)). Outside the core window with increasing distance all magnetic fields show a monotonic decay to zero.

The resulting magnetic field H_{r} is calculated by superposition of $H_{\mathrm{r},1}$ and $H_{\mathrm{r},2}$, or could also be directly derived from Ampère's law. As shown in Fig. 4, the derived magnetic field distribution is verified by FEM-simulation. For both, simulation and calculation, it is assumed that $N_1 I_1 > N_2 I_2$, which is always the case for transformers with low magnetic coupling and resistive loads, since the primary source has to deliver the active power for the load and the reactive power of the transformer. Therefore, $N_1 I_1 = N_2 I_2$ can only be assumed for transformers with a high magnetic coupling and a high magnetizing inductance. However, as will be shown later, depending on the load behavior it is also possible that $N_1 I_1 < N_2 I_2$; the magnetic field distribution is significantly influenced by the load.

For the sake of completeness, if $r_1 \gg (r_2 - r_1)$ is not true, the magnetic field is depending on the radius r: $H_{\mathrm{r}}(r) = \phi / (\mu_0 2\pi r)$, whereas ϕ is derived based on Ampère's law,

$$\Theta = \int_{r_1}^{r_2} H_{\mathrm{r}}(r)\mathrm{d}r = \frac{\phi}{\mu_0 2\pi} \cdot \ln\left(\frac{r_2}{r_1}\right) \Rightarrow H_{\mathrm{r}}(r) = \frac{\Theta}{r \cdot ln\left(\frac{r_2}{r_1}\right)}, \quad (1)$$

where Θ is the magnetomotive force which equals the total ampere-turns enclosed by the loop path.

With the derived magnetic field distribution and the given cross section of concept 1, the corresponding reluctance model is deduced, which describes the magnetic properties of concept 1. Since both, the magnetic flux ϕ and flux density B, show the same direction as the magnetic field H, in the reluctance model only reluctances in r-direction are used. There, each reluctance is defining the magnetic flux portion which is flowing through a certain area of the cross section. For concept 1, the total magnetic flux is split into a flux

portion (fringing flux) outside the core window, which is considered with the reluctance R_f, and a flux portion inside the core window. The flux portion inside the core window is further split into three flux portions, where the fluxes flowing through the primary or secondary winding are described with the reluctances R_sp and R_a respectively, and the flux flowing in between the two windings is considered with the reluctance R_s (cf. Fig. 3 c)).

In the reluctance model the spatial arrangement of the primary winding over the winding length l_w1 and of the secondary winding over the winding length l_w2 has to be considered. Therefore, to get an accurate description of the magnetic behavior, the magnetomotive forces (MMFs) Θ_1 and Θ_2 are split into k_1 and k_2 series connected portions $\Theta_{1,\mathrm{i}} = N_1 I_1/k_1$ and $\Theta_{2,\mathrm{i}} = N_2 I_2/k_2$ respectively. For this reason also the reluctances R_sp and R_a have to be split into k_1 and k_2 parallel reluctances $R_{\mathrm{sp,i}} = k_1 \cdot R_\mathrm{sp}$ and $R_{\mathrm{a,i}} = k_2 \cdot R_\mathrm{a}$ respectively as shown in Fig. 5 a).

Since the derived reluctance model is impractical for the calculation of the magnetic behavior, the distributed reluctances $R_{\mathrm{sp,i}}$ and $R_{\mathrm{a,i}}$ as well as the distributed MMFs $\Theta_{1,\mathrm{i}}$ and $\Theta_{2,\mathrm{i}}$ are summarized again, resulting in a lumped equivalent reluctance model. For example, to calculate the equivalent reluctance $R_{\mathrm{a,eq}}$ of the distributed reluctances $R_{\mathrm{a,i}}$ the magnetic voltage source Θ_1 has to be shorted out ($I_1 = 0$) which leads to the reluctance model shown in Fig. 5 c). There, on one side all distributed reluctances $R_{\mathrm{a,i}}$ are connected to the ground potential and on the other side to the voltage $i \cdot \Theta_{2,\mathrm{i}}$. This arrangement of reluctances $R_{\mathrm{a,i}}$ and MMFs $\Theta_{2,\mathrm{i}}$ can be simplified to one reluctance $R_{\mathrm{a,eq}}$ which is only connected to Θ_2, where it has to be guaranteed that the total flux for both circuits is the same, i.e. $\phi_{2,1} + \phi_{2,2} + \phi_{2,3} + ... = \phi_{2,\mathrm{eq}}$. According to (2), this results in $R_{\mathrm{a,eq}} = 2R_\mathrm{a}$.

$$\sum_{i=1}^{k_2} \phi_{2,i} = \sum_{i=1}^{k_2} \frac{(\frac{I_2 N_2 \cdot i}{k_2})}{k_2 \cdot R_\mathrm{a}} = \frac{I_2 N_2}{k_2^2 R_\mathrm{a}} \sum_{i=1}^{k_2} i = \frac{I_2 N_2}{2R_\mathrm{a}} \stackrel{!}{=} \frac{I_2 N_2}{R_{\mathrm{a,eq}}} \qquad (2)$$

As was shown in Fig. 3 c), however, the reluctance of the air gap over the length l_w2 is R_a, which is also found with the reluctance

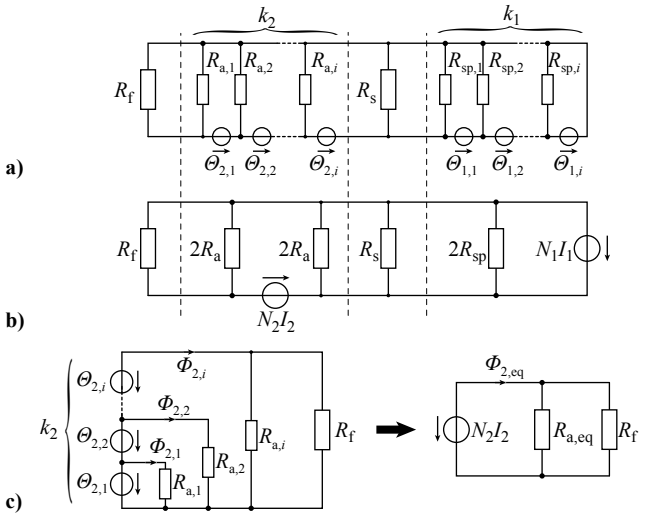

Fig. 5. Description of magnetic behavior of concept 1 based on a) reluctance model with distributed reluctances $R_{\mathrm{sp,i}}$ and $R_{\mathrm{a,i}}$ and distributed magnetomotive forces MMFs $\Theta_{1,\mathrm{i}}$ and $\Theta_{2,\mathrm{i}}$, b) lumped reluctance model and c) simplification of the reluctance model by summarizing the distributed reluctances.

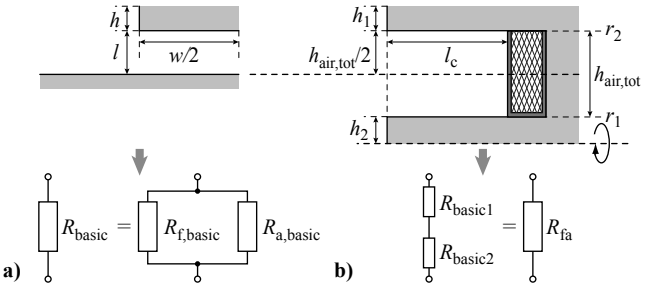

Fig. 6. Calculation of 3D-reluctance of the fringing flux R_f^3D based on the analysis detailed in [10] by describing a complex air gap geometry with an assembly of basic geometries.

model in Fig. 5 a), if the MMF Θ_2 is shorted out ($I_2 = 0$). This means that for concept 1 the secondary winding is only coupled with half of the primary flux within l_w2; this could also be calculated by summing up the induced voltages in each secondary's turn. As a consequence, this results in a low magnetic coupling of the two windings. In the reluctance model for concept 1, this fact has to be considered by splitting the reluctance R_a into two parallel reluctances $2R_\mathrm{a}$, whereas the secondary winding's MMF Θ_2 has to be placed in between these two reluctances (cf. Fig. 5 b)).

The distributed reluctances $R_{\mathrm{sp,i}}$ can be summarized based on the same procedure, shorting out Θ_2 ($I_2 = 0$), resulting in a equivalent reluctance $R_{\mathrm{sp,eq}} = 2R_\mathrm{sp}$ as shown in Fig. 5 b).

The reluctance values of the simplified reluctance model for concept 1 can be derived from the dimensions of the corresponding cross section. The 2D-reluctances R_a, R_s and R_sp inside the core window can be easily calculated by

$$R_\mathrm{x}^\mathrm{2D} = \frac{l_x}{\mu_0 \cdot h_{\mathrm{air,tot}}} \qquad (3)$$

where l_x has to be adapted to the corresponding dimension: l_w2 for R_a^2D, l_s for R_s^2D and l_w1 for $R_\mathrm{sp}^\mathrm{2D}$. For $(r_2 - r_1) \ll r_1$, as a good approximation, the 3D-reluctance can be calculated by multiplying the 2D-reluctance with the average circumference of the air gap $r_\mathrm{avg} = (r_2 + r_1)/2$. The accurate calculation of the 3D-reluctance results in

$$R_\mathrm{x}^\mathrm{3D} = \frac{1}{2\pi \cdot \mu_0 \cdot l_x} \ln(\frac{r_\mathrm{a}}{r_\mathrm{i}}). \qquad (4)$$

The 3D-reluctance R_f^3D of the fringing flux is derived based on the analysis in [10], whereas first the corresponding 2D-reluctance R_f^2D has to be determined. As shown in [10], the reluctance of a complex air gap geometry can be substituted by an assembly of basic geometries (cf. Fig. 6 a)), whose 2D-reluctance is calculated based on the conformal Schwarz-Christoffel transformation;

$$R_\mathrm{basic}^\mathrm{2D} = \frac{1}{\mu_0[\frac{w}{2l} + \frac{2}{\pi}(1 + \ln(\frac{\pi h}{4l}))]}. \qquad (5)$$

The air gap geometry of concept 1 can be realized with two basic geometries which are lying upon another as shown in Fig. 6 b). Thus, the reluctance $R_\mathrm{fa}^\mathrm{2D}$ of the air gap of concept 1 is equal to the series connection of the two basic reluctances $R_{\mathrm{basic,1}}^\mathrm{2D}$ and $R_{\mathrm{basic,2}}^\mathrm{2D}$, where the corresponding dimensions $l = h_{air,tot}/2$ and $w/2 = l_c$ for both reluctances, $h = h_1$ for $R_{\mathrm{basic,1}}^\mathrm{2D}$ and $h = h_2$ for $R_{\mathrm{basic,2}}^\mathrm{2D}$ have to be considered.

The calculated reluctance $R_\mathrm{fa}^\mathrm{2D}$ includes the reluctance R_f of the fringing flux outside the core window and the reluctance R_a^2D of

the flux inside the core window over the length l_c. Since the 2D-reluctance R_a^2D is given by (3), R_f^2D can be deduced from $R_\mathrm{fa}^\mathrm{2D}$ and R_a^2D,

$$R_\mathrm{f}^\mathrm{2D} = \frac{R_\mathrm{fa}^\mathrm{2D} R_\mathrm{a}^\mathrm{2D}}{R_\mathrm{a}^\mathrm{2D} - R_\mathrm{fa}^\mathrm{2D}}. \tag{6}$$

The impact of the fringing field on the total flux can be described with the fringing factor σ^2D, introduced in [10], which is just the ratio of the two 2D-reluctances $R_\mathrm{fa}^\mathrm{2D}$ and R_a^2D, where the fringing field of the air gap is either considered or neglected,

$$\sigma^\mathrm{2D} = \frac{R_\mathrm{fa}^\mathrm{2D}}{R_\mathrm{a}^\mathrm{2D}} = \frac{R_\mathrm{f}^\mathrm{2D}}{R_\mathrm{f}^\mathrm{2D} + R_\mathrm{a}^\mathrm{2D}}. \tag{7}$$

As a result, for $\sigma^\mathrm{2D} \approx 1$ the fringing flux can be neglected and for decreasing values of σ^{2D} the impact of the fringing flux is increasing. Due to the cylindrical shape of the proposed rotary transformer concepts, this fringing factor σ^2D can now be used to calculate the 3D-reluctance R_f^2D of the fringing flux, since in this case the 2D- and 3D-fringing factor are the same. Thus, the 3D-reluctance R_f^3D is found as

$$R_\mathrm{f}^\mathrm{3D} = \frac{\sigma^\mathrm{2D} R_\mathrm{a}^\mathrm{3D}}{1 - \sigma^\mathrm{2D}}. \tag{8}$$

With the calculated 3D-reluctances R_f^3D, R_a^3D, R_s^3D and $R_\mathrm{sp}^\mathrm{3D}$ the magnetic behavior of concept 1 is fully described. However, instead of the reluctance model, the magnetic behavior of a transformer is usually described with the general transformer model, shown in Fig. 7 a), consisting of the two self-inductances L_1 and L_2 and the mutual inductance M. These values can be directly deduced from the corresponding reluctance model.

In order to calculate the self-inductances L_1 and L_2 either the secondary winding (for L_1) or the primary winding (for L_2) has to be shorted out in the reluctance model. The sum of the remaining reluctances leads to the corresponding self-inductance L_1 or L_2,

$$L_1 = \frac{N_1^2}{R_\mathrm{f}||R_\mathrm{a}||R_\mathrm{s}||2 \cdot R_\mathrm{sp}} \quad \text{and} \quad L_2 = \frac{N_2^2}{R_\mathrm{f}||2 \cdot R_\mathrm{a}}. \tag{9}$$

For the calculation of the mutual inductance M also the voltage transfer ratio V_2/V_1 is needed, which is - due to the low magnetic coupling - not equal to the turns ratio N_2/N_1. However, the voltage transfer ratio V_2/V_1 is given by the reluctances $R_\mathrm{gen,h}$ and $R_\mathrm{gen,s}$ of the two winding transformer's general reluctance model (cf. Fig. 7 b)),

$$M = \frac{V_2}{V_1} \cdot L_1 = \frac{N_2}{N_1} \cdot \frac{R_\mathrm{g,s} \cdot R_\mathrm{g,h}}{R_\mathrm{g,s} + R_\mathrm{g,h}} \cdot L_1. \tag{10}$$

For concept 1 this results in $R_\mathrm{g,s} = 2R_\mathrm{a}||R_\mathrm{s}||2R_\mathrm{sp}$ and $R_\mathrm{g,h} = R_\mathrm{f}||2R_\mathrm{a}$.

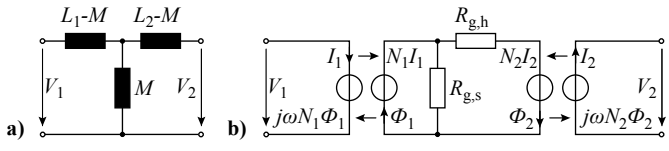

Fig. 7. a) General transformer model defined by the two self-inductances L_1 and L_2 and the mutual inductance M, b) general reluctance model of a two winding transformer coupled with the electrical circuit in order to calculate the voltage transfer ratio V_2/V_1.

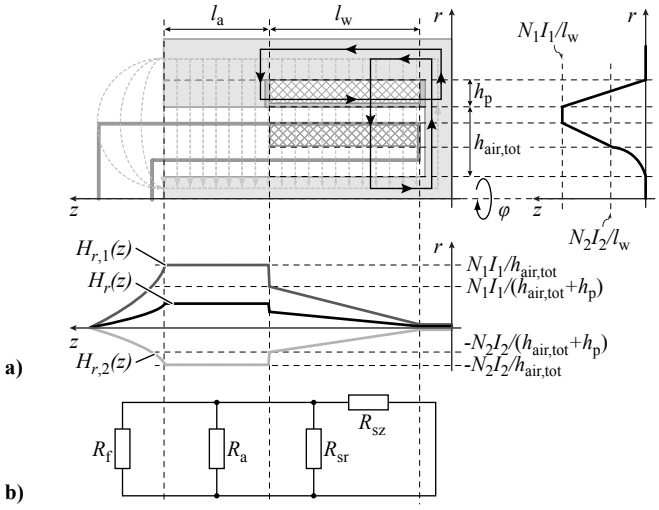

Fig. 8. a) Dimensions of the rotary transformer (drawing not to scale) and schematic H-field distributions $H_\mathrm{r}(z)$ and $H_\mathrm{z}(r)$ and b) magnetic reluctances of concept 2.

In order to improve the magnetic coupling, in concept 2 the stationary primary winding is placed around the rotating secondary winding, both having an equal winding length l_w (cf. Fig. 8 a)). Additionally, a separate air gap l_a is inserted, thus, in contrast to concept 1 almost all turns of the secondary winding are linked with the whole primary's magnetic flux. However, due to the modified winding arrangement, the derivation of the magnetic field's distribution is difficult, since between the two windings of concept 2 the magnetic field H has a r- and a z-component.

In Fig. 8 a) the cross section of concept 2 and the resulting magnetic field, separated in r- and z-direction, is illustrated. The distribution of $H_\mathrm{r}(z)$ and $H_\mathrm{z}(r)$ can be deduced from Ampère's law again, however, for each magnetic field's component a separate rectangular closed loop path is used (cf. Fig. 8 a)).

As was already shown for concept 1, the distribution of the magnetic field in radial direction $H_\mathrm{r}(z)$ is found by continuously increasing the loop path's width in z-direction, hence, continuously enclosing more and more turns of the primary and secondary winding. This leads to linearly increasing magnitude of $H_\mathrm{r}(z)$ inside the core window l_w (assuming again $N_1 I_1 > N_2 I_2$) whose maximum is $(N_1 I_1 - N_2 I_2)/(h_\mathrm{air,tot} + h_\mathrm{p})$. In the air gap width l_a the magnetic field has only a radial component, which is constant and, due to the smaller air gap, higher than in the winding window $(N_1 I_1 - N_2 I_2)/(h_\mathrm{air,tot})$. Outside the air gap the field monotonically decays to zero again.

The z-component $H_\mathrm{z}(r)$ is determined with a second loop path having a constant width l_w and a continuously increasing height in r-direction. Inside the stationary primary winding $H_\mathrm{z}(r)$ linearly increases to $N_1 I_1/l_\mathrm{w}$, stays constant between the two windings and decreases linearly inside the secondary winding to $(N_1 I_1 - N_2 I_2)/l_\mathrm{w}$. Between the secondary winding and the middle limb of the pot core the magnetic field $H_\mathrm{z}(r)$ decreases to zero.

At any position inside the core window, the magnetic field H can be calculated by the superposition of $H_\mathrm{r}(z)$ and $H_\mathrm{z}(r)$. For example, the magnetic field H along the secondary winding shows a constant z-component and a linearly increasing r-component resulting in a rotation of the magnetic field vector which is verified by FEM-simulations (cf. Fig. 9).

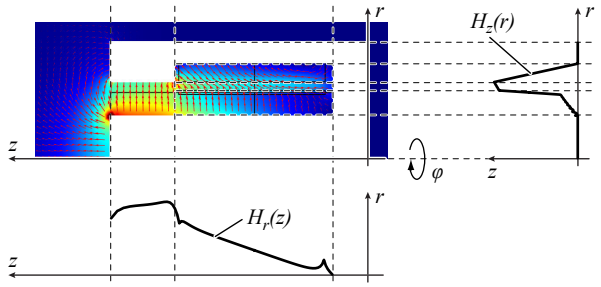

Fig. 9. FEM-simulation of the magnetic field components $H_\mathrm{r}(z)$ and $H_\mathrm{z}(r)$ for concept 2.

The magnetic behavior of concept 2 can also be described with the corresponding reluctance model. There, the flux in the air gap is considered with the reluctance R_a and the fringing flux outside the pot core with the reluctance R_f, both only in r-direction. Inside the core window, the magnetic flux between the two windings has to be modeled with the two reluctances R_sr in r-direction and R_sz in z-direction. Since the primary and secondary winding are again spatially arranged over the winding length l_w, the MMFs Θ_1 and Θ_2 are split into k_3 distributed MMFs $\Theta_{1,i} = \Theta_1/k_3$ and $\Theta_{2,i} = \Theta_2/k_3$ as well as the two reluctances R_sr and R_sz into k_3 distributed reluctances $R_{\mathrm{sr},i} = k_3 R_\mathrm{sr}$ and $R_{\mathrm{sz},i} = k_3 R_\mathrm{sz}$ (cf. Fig. 10 a)).

As shown with concept 1, the reluctance model of concept 2 can be simplified by summarizing the distributed reluctances $R_{\mathrm{sr},i}$ and $R_{\mathrm{sz},i}$ - shoring out Θ_1 or Θ_2 - which leads to the lumped reluctance model shown in Fig. 10 b). Depending on the mechanical dimensions the corresponding reluctance values are calculated based on (4) and (8). Instead of the reluctance model, the magnetic behavior of a transformer is again described with the general transformer model. The two self-inductances L_1 and L_2 are

$$L_1 = \frac{N_1^2}{R_\mathrm{f}||R_\mathrm{a}||R_\mathrm{s}||2\cdot R_\mathrm{sp}} \quad \text{and} \quad L_2 = \frac{N_2^2}{R_\mathrm{f}||2\cdot R_\mathrm{a}}. \tag{11}$$

The mutual inductance M of concept 2 is again determined by the voltage transfer ratio V_2/V_1 which is calculated based on the two reluctances $R_{\mathrm{g,s}} = R_\mathrm{sz}||2R_\mathrm{sp}$ and $R_{\mathrm{g,h}} = R_\mathrm{f}||R_\mathrm{a}||2R_\mathrm{sr}$.

IV. Electrical Design

In addition to the magnetic behavior, also the electrical design of the rotary transformer concepts is presented. For the winding losses, the skin and proximity-effects have to be considered, since

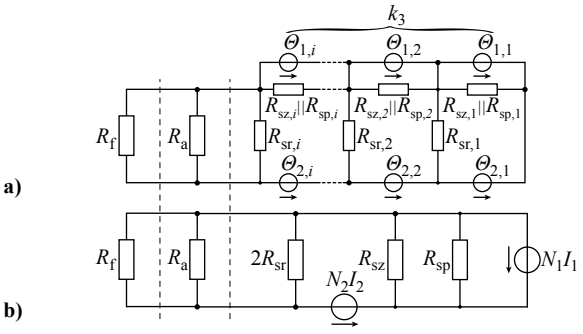

Fig. 10. Description of magnetic behavior of concept 2 based on a) reluctance model with distributed reluctances $R_{\mathrm{sp,i}}$ $R_{\mathrm{sz,i}}$ and $R_{\mathrm{sr,i}}$ and distributed MMFs $\Theta_{1,\mathrm{i}}$ and $\Theta_{2,\mathrm{i}}$ and b) lumped reluctance model.

the electrical frequency and the H-field in the air gap can be high. In many applications a high electrical frequency is selected in order to make the transformer small, which is also desired for the proposed rotary transformer concepts in high-speed applications, since with smaller cross sections and/or circumferences also the centripetal forces are decreased. However, in ultrasonic applications, like in grinding processes of hard ceramics, the piezo-electric resonator has to be operated at its mechanical resonance frequency. Thus, for these applications (pure sinusoidal waveforms) the electrical frequency is already determined, which is in this case 70 kHz. However, the electrical analysis can also be performed for non-sinusoidal waveforms based on a Fourier series calculating the losses for each harmonic component.

A. Winding Losses

The influence of the skin and proximity-effects (eddy currents induced by an ext. field) on the winding losses at a certain excitation frequency can be expressed with the two coefficients F and G respectively, which can be translated into an increase of the conductor's DC-resistance $R_{\mathrm{w,DC}}$ and thus to higher winding losses [11], [12].

$$P_{\mathrm{w},i} = R_{\mathrm{w,DC}} \cdot F \cdot \hat{I}_i^{\,2} + R_{\mathrm{w,DC}} \cdot G \cdot \hat{H}_{\mathrm{ext}}^2. \tag{12}$$

There, the coefficients F and G only depend on the conductor material, the selected conductor type (solid wire, stranded wire, or foil) and the excitation frequency. The accurate calculation of these coefficients is found in [11], [12]. Since for the primary and secondary winding different conductor types can be used and the current rating I_i as well as the external magnetic H_ext are different, the losses have to be calculated separately for each winding. In addition, usually H_ext is varying over the winding length. Therefore, the winding losses per turn have to be calculated which are then summarized in order to determine the total winding losses. The difficulty of the winding loss calculation is mainly the determination of the magnetic field distribution $H_\mathrm{ext}(r, z, \phi)$ inside the windings. The magnetic field distributions for the proposed rotary transformer concepts, however, were already derived in the previous section.

Due to the relatively large air gap $h_{\mathrm{air,tot}}$ of the proposed rotary transformer concepts only small self-inductances are achieved. Additionally, the winding arrangement of concept 1 results in a low magnetic coupling. Therefore, the electrical source on the primary side has to deliver the active power for the load (assuming a purely resistive load) and the reactive power drawn from the rotary transformer which can be dominant. Consequently, the electrical source has to be over-designed. This is true even for the rotary transformer, since the needed magnetizing current leads to a higher current rating of the primary winding (losses due to skin effect increase) and to a higher magnetic field's magnitude which increases the losses due to proximity effect in both windings. In Fig. 11 a) the electric circuit with a purely resistive load R_L (output power: 200 W, output voltage: 1000 V) for the built prototype of concept 1 and the corresponding distribution of the magnetic field (n.c.) is shown. Inside the primary winding the magnetic field's magnitude is steeply increasing; due to the fact that $N_1 I_1 \gg N_2 I_2$, inside the secondary winding it is only slowly decreasing.

To reduce the apparent power of the source, one could think to choose a higher number of turns N_1 and N_2 in order to increase the self-inductance. However, due to the small dimensions of the rotary transformer, considering mechanical forces the space for the windings is limited. Therefore, increasing the number of turns would result in a lower primary current but also in a disproportional

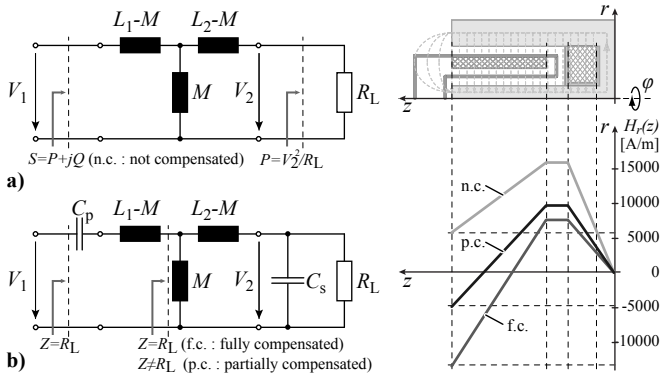

Fig. 11. a) Electrical circuit with resistive load (not compensated) b) compensation of reactive power with additional capacitors C_p and C_s (fully and partally compensated, with $C_\mathrm{p} = 835\,\mathrm{pF}, C_\mathrm{s} = 1\,\mu\mathrm{F}$ and $C_\mathrm{p} = 475\,\mathrm{pF}, C_\mathrm{s} = 0.37\,\mu\mathrm{F}$ respectively) and corresponding runs of the magnetic field.

higher DC-resistance of the winding. Additionally, the magnetic field is proportionally reduced with I_i, however, increases with N_i. Nevertheless, an optimum of the transformer design for a resistive load can be found.

Instead of adjusting the number of turns, the apparent power drawn from the source as well as the generated losses in the transformer can be significantly influenced by the load. For example, the reactive power of the transformer can be fully compensated with a capacitor C_p parallel to the load resistor R_L, to compensate the self-inductance L_2, and a capacitor C_s in series to the transformer's primary winding, to compensate the primary's leakage inductance as shown in Fig. 11 b), whereas the capacitor values are calculated according to (13). For the sake of completeness, also other arrangements of compensation capacitors would be possible: parallel-parallel, series-series and parallel-series. Usually the capacitor arrangement with the most reasonable capacitor values is selected,

$$C_\mathrm{p} = \frac{1}{(2\pi f_\mathrm{elec})^2 \cdot L_2} \quad \text{and} \quad C_\mathrm{s} = \frac{1}{(2\pi f_\mathrm{elec})^2 \cdot (L_1 - M)}. \tag{13}$$

As a result, the electrical source only has to deliver the active power for the load R_L; the reactive power is fully carried by the compensation capacitor C_p on the secondary side. This completely changes the distribution of the magnetic field, since now $N_2 I_2 \gg N_1 I_1$ (cf. Fig. 11). As can be noticed, the magnetic field in the air gap is now changing its direction. The power demand and HF-losses on the primary are drastically reduced. On the secondary, however, the losses are increased again by approximately the same amount.

Both described possibilities (not compensated and fully compensated) are extreme cases where the whole reactive power is either covered from the primary or secondary side. In order to improve the current and magnetic field distribution, which would result in reduced total winding losses, the reactive power can also be shared to both windings. Therefore, the value of C_p, which was found according to (13), is continuously reduced; thus, more and more reactive power is drawn from the primary since the self-inductance L_2 is only partially compensated by C_p. However, the increasing reactive power drawn from the primary can again be compensated with an appropriate capacitance C_s in such a way the that total impedance seen from the source is still purely resistive. For each combination of C_p and C_s, with the given load specification and the magnetic behavior of the rotary transformer, the primary and secondary currents and the magnetic field distribution can be calculated. With this iteration the best combination of C_p and C_s resulting in the lowest total losses can be found. However, for the optimal compensation also the resulting core losses have to be considered, which is done in the following subsection.

Instead of adjusting the capacitors to the given magnetic behavior of the transformer, with a piezo-electric resonator, which is already a capacitive load, the transformer could be designed in such a way that the resonator's capacitance can be directly used for proper compensation on the secondary side. Hence, a low magnetic coupling is even desired in order to compensate the reactive power drawn from the capacitive load.

In Fig. 11 the distribution of the magnetic field with optimal compensation is shown. It has to be mentioned that for the calculated magnetic field distributions a constant output power and output voltage are assumed. Since the transfer ratio of the circuit will change depending on the selected capacitor values C_p and C_s, the primary current I_1 and the magnetic field generated by the primary winding will also change even if the input power stays constant.

It also has to be mentioned that in transformers with low self-inductances and low magnetic coupling the primary and secondary current and consequently also the magnetic fields $H_{\mathrm{r},1}(z) = |H_{\mathrm{r},1}(z)| \cdot \cos(\omega t + \varphi_{H,1})$ and $H_{\mathrm{r},2}(z) = |H_{\mathrm{r},2}(z)| \cdot \cos(\omega t + \varphi_{H,2})$ are not in phase with each other, which means $\varphi_{H,1} \neq \varphi_{H,2}$. For large phase differences this can result in significant errors if for the magnetic field distribution only the magnitudes of the magnetic fields $H_{\mathrm{r},1}(z)$ and $H_{\mathrm{r},2}(z)$ are considered. For the prototype of concept 1 with optimal compensation, the phase difference of the magnetic fields $H_{\mathrm{r},1}(z)$ and $H_{\mathrm{r},2}(z)$ is almost $90\,^\circ$. If one would calculate the difference of the magnitudes, this would always result in a value which is smaller than the magnitude of the larger field vector. However, with a phase difference of almost $90\,^\circ$ this leads to a value which is even bigger than the magnitude of the larger field vector.

The same considerations have to be done for concept 2, whereas the two magnetic field components in r- and z-direction can be considered separately due to the orthogonality principle. However, the phase difference of the primary and secondary current has to be considered for both field components.

B. Core Losses

As was already mentioned, in ultrasonic applications the piezo-electric resonator is operated at its mechanical resonance frequency with a purely sinusoidal waveform, which allows the calculation of the core losses per volume P_c based on the Steinmetz equation,

$$P_\mathrm{c} = k \cdot f^\alpha \cdot \hat{B}^\beta, \tag{14}$$

where f is the excitation frequency, $\hat{B}$ is the peak flux density and k, α and β are the Steinmetz parameters which are found by curve fitting of datasheet values. For a non-sinusoidal flux density waveforms the improved generalized Steinmetz equation proposed in [13] has to be used.

Due to the constant frequency of the underlying application the term f^α can be merged with the parameter k. Thus, the core losses are only depending on the peak flux density $\hat{B}$. For the proposed rotary transformer concepts the flux density $\hat{B}$ in the stationary pot core is not constant, however, the flux density distribution can be deduced from the derived magnetic field distribution in the air gap. The flux density inside core window is proportional to the corresponding magnetic field H_r which is $B_{\mathrm{r,a}} = \mu_0 \cdot H_r$ and only has a radial direction for concept 1 and additionally a z-direction

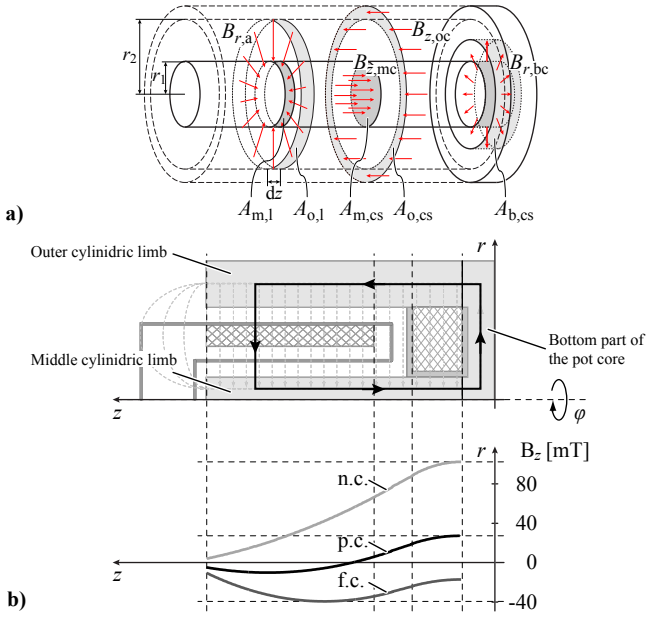

Fig. 12. a) Schematic view of the flux densities inside the air gap and the pot core with the corresponding cross sections, b) the resulting flux density profile $B_{\mathrm{z,mc}}(z)$ in the middle limb of concept 1 for non, full and partial capacitive compensation.

for concept 2. In order to calculate the flux density in the core material, the pot core is split into three parts, an outer and middle cylindric limb and a bottom core part (cf. Fig. 12 b)), where it is assumed that the flux densities $B_{\mathrm{z,oc}}$ and $B_{\mathrm{z,mc}}$ in the outer and middle cylindrical limbs have only a z-direction and the flux density $B_{\mathrm{r,bc}}$ in the bottom part has only a radial direction. As shown in Fig. 12 a), the magnetic field in the air gap enters the middle limb radially through the lateral area $A_{\mathrm{m,l}} = 2\pi r_1 \cdot \mathrm{d}z$ with an infinitesimal width $\mathrm{d}z$ resulting in a magnetic flux change $\mathrm{d}\phi = B_{\mathrm{r,a}} \cdot A_{\mathrm{m,l}}$. The same magnetic flux change $\mathrm{d}\phi$ is penetrating the middle limb in z-direction and is assumed to be uniformly distributed over the area $A_{\mathrm{m,cs}}$. Consequently, the change in flux density in the middle limb is calculated as

$$\mathrm{d}B_{\mathrm{z,mc}} = \frac{\mathrm{d}\phi}{A_{\mathrm{m,cs}}} = \frac{2\pi r_1 \cdot \mu_0 H_{\mathrm{r,a}}(r)}{A_{\mathrm{m,cs}}} \mathrm{d}z. \tag{15}$$

Since the magnetic field in the air gap H_{r} is entering the middle limb over the whole length l_c, the distribution of the flux density inside the middle core $B_{\mathrm{z,mc}}(z)$ is found by integration of $\mathrm{d}B_{\mathrm{z,mc}}$. Additionally, the magnetic flux in the fringing field $\phi_{\mathrm{f}} = (N_1 I_1 - N_2 I_2)/R_{\mathrm{f}}$ has to be considered,

$$B_{\mathrm{z,mc}}(z) = \int_0^z \frac{2\pi r_1 \cdot \mu_0 H_{\mathrm{r,a}}(r)}{A_{\mathrm{m,cs}}} \mathrm{d}z + \frac{\phi_{\mathrm{f}}}{A_{\mathrm{m,cs}}}. \tag{16}$$

In Fig. 12 b) the resulting flux density $B_{\mathrm{z,mc}}(z)$ in the middle limb for concept 1 and for the three presented capacitive compensation options, i.e. not compensated, fully compensated and partially compensated, is shown. Since the capacitive compensation is influencing the magnetic field in the air gap H_{r} also the distribution of the flux density $B_{\mathrm{z,mc}}(z)$ in the core material is changed. As can be noticed, with optimal compensation not only H_{r} is changing the direction inside the air gap but also the flux density $B_{\mathrm{z,mc}}(z)$.

The flux density $B_{\mathrm{z,oc}}(z)$ in the outer cylindrical limb has the same flux distribution as $B_{\mathrm{z,mc}}(z)$, whereas the core cross section $A_{\mathrm{o,cs}}$ instead of $A_{\mathrm{m,cs}}$ has to be used. In the bottom part of the pot core the magnetic flux ϕ is constant. The cross section $A_{\mathrm{a,cs}}$ in radial direction, however, is linearly increasing. Thus, the flux density $B_{\mathrm{r,bc}}(r)$ is proportional to $1/r$.

With the calculated flux densities in all three parts of the pot core, the core losses can be calculated according to (14). The same procedure is applied to concept 2 where both magnetic field components $H_z(r)$ and $H_{\mathrm{r}}(z)$ in the air gap have to be considered.

V. Mechanical Design

Besides the magnetic and electrical design also a proper mechanical analysis is needed. For the mechanical design the rotor dynamics, i.e bending vibrations at the resonance frequencies and the centrifugal forces, and a stress analysis for the different materials have to be considered. For the estimation of the centrifugal forces a two dimensional analytical analysis according to [14] is carried out. There, the tangential stresses should be well below the tensile yield strength of the materials. Concerning rotor dynamics, for safe operation, the resonant frequencies of the rotor (including spindle and transformer) must be higher than the maximum fundamental rotational frequency of the rotor. The resonant frequencies are computed using a one dimensional numerical model based on the Euler-Bernoulli beam [15].

VI. Experimental Measurements

In Fig. 13 the exploded views of both rotary transformer prototypes are shown. The transformers were designed for an output power of 200 W, an electrical frequency of 70 kHz, and a rotational speed of 60′000 rpm.

As shown in Table I, the calculated self-inductances L_1 and L_2 for both concepts based on the derived reluctance models only differ slightly ($< 10\,\%$) from the measured values.

In Table II the calculated losses in the winding and the core material for both concepts are listed. For both concepts almost the same total losses are calculated.

For the mechanical design the tangential stresses in the copper winding and the winding bobbin made of PEEK were calculated (for

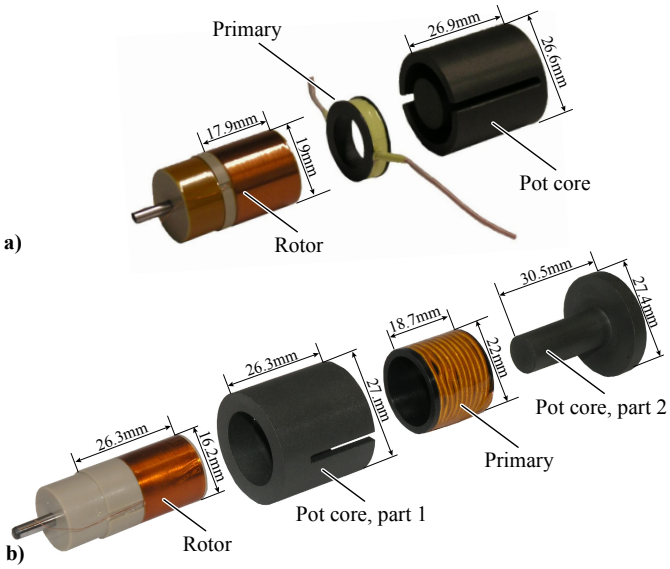

Fig. 13. Realized prototype of a) concept 1 with $N_1 = 6$, $N2 = 202$ and b) concept 2 with $N_1 = 10$, $N2 = 200$.

TABLE I
COMPARISON OF CALCULATED AND MEASURED INDUCTANCE VALUES FOR BOTH ROTARY TRANSFORMER CONCEPTS.

	Calculated	*Measured*	*Relative Error*
L_1 of concept 1	13.9 µH	14.0 µH	−0.2 %
L_2 of concept 1	7.1 mH	6.5 mH	9.7 %
L_1 of concept 2	23.3 µH	25.5 µH	−8.6 %
L_2 of concept 2	8.6 mH	8.3 mH	3.6 %

TABLE II
COMPARISON OF CALCULATED LOSSES FOR BOTH ROTARY TRANSFORMER CONCEPTS.

	Concept 1	*Concept 2*
Losses in primary winding	0.5 W	0.25 W
Losses in secondary winding	0.3 W	0.6 W
Core losses	1.65 W	1.2 W
Total losses	2.45 W	2.05 W

concept 1 / 2: 33 MPa / 26.7 MPa in the copper winding and 4 MPa / 3.1 MPa in the PEEK bobbin), which are expected to be less than 10 % of the tensile yield strength of the materials. Moreover it is found that already a small preload of approx. 1 N is sufficient while winding the copper wire on the bobbin in order to prevent the winding from lifting off during operation.

For both concepts the first resonant frequency of the rotor (including the spindle) is expected to be at 2.6 kHz which corresponds to a rotational speed of 156'000 rpm. The reason can be found in the lightweight and small construction of the rotary transformers; the rotor's weight for concept 1 is only 8 g and for concept 2 it is 6 g. Thus, due to the much larger dimensions and weight of the grinding spindle, the influence of the rotary transformer on the mechanical behavior is small. This was also verified with an over-speed test as shown in Fig. 14, where the vibration velocity was measured for both concepts for different rotational speeds up to 60′000 rpm without balancing the rotor. Also a reference measurement without any rotary transformer was performed. As can be noticed, the vibration velocity, is only slightly changed with attached transformer and is well below 3 mm/s, which is the maximum allowed velocity of the used grinding spindles.

VII. CONCLUSION

Due to the rotating core material and its limited mechanical strength, conventional rotary transformer concepts are not suitable for high-speed applications. Therefore, two rotary transformer concepts, where no magnetic material is employed on the rotating part, are analyzed in this paper. These concepts feature a simple and mechanical robust design with a lightweight construction resulting in very small unbalanced mass. In the paper a detailed magnetic, electrical and, mechanical analysis of the proposed rotary transformer concepts is presented. The feasibility and performance of the concepts are proved with experimental results of a built prototype. Both concepts show a similar mechanical and electrical behavior. Due to an improved winding arrangement concept 2 features a higher magnetic coupling compared to concept 1. This, however, can be compensated with additional capacitors. Concerning costs, since for concept 2 two separate core parts are needed, the manufacturing of concept 2 is more expensive. Accordingly, in a first step concept 1 should be considered for an industrial application.

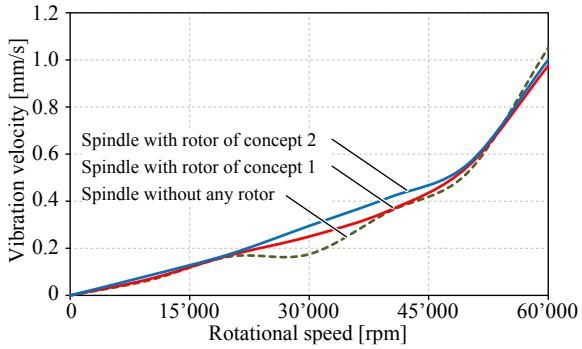

Fig. 14. Measured vibration velocity in the performed over-speed test for both transformer concepts and without any transformer.

ACKNOWLEDGMENT

The authors would like to thank Mr. Iseli from Fischer AG (www.fischerprecise.ch) who performed the over-speed tests.

REFERENCES

[1] I. D. Marinescu, M. Hitchiner, E. Uhlmann, W. B. Rowe, and I. Inasaki, "Handbook of Machining with Grinding Wheels," Pages 549-562, CRC Press 2006.

[2] E. Uhlmann, and C. Huebert, "Ultrasonic Assisted Grinding of Advanced Ceramics," *Proceedings of the Annual Meeting of the American Society for Precision Engineering*, Atlanta, GA, Nov 2007.

[3] B. Lauwers, F. Bleicher, P. Ten Haaf, M. Vanparys, J. Bernreiter, T. Jacobs, and J. Loenders, "Investigation of the Process-Material Interaction in Ultrasonic Assisted Grinding of ZrO2 based Ceramic Materials," *Proceedings of 4th CIRP International Conference on High Performance Cutting*, 2010.

[4] C. WM. T. McLyman, "Transformer and Inductor Design Handbook," Third Edition, Revised and Expanded, Pages 19.3-19.10, New York, NY, Marcel Dekker, Inc., 2004.

[5] B. A. Potter, and S. A. Shirsavar, "Design, Implementation and Characterisation of a Contactless Power Transfer System for Rotating Applications," *Proceedings of the 32th Annual Conference on IEEE Industrial Electronics*, pp. 2168-2173, Nov. 2006.

[6] K. D. Papastergiou, and D. E. Macpherson, "An Airborne Radar Power Supply With Contactless Transfer of Energy-Part I: Rotating Transformer," *IEEE Transactions on Industrial Electronics*, vol. 54, no. 5, Oct. 2007.

[7] J. P. C. Smeets, L. Encica and, E. A. Lomonova, "Comparison of Winding Topologies in a Pot Core Rotating Transformer," *Proceedings of the 12th International Conference on Optimization of Electrical and Electronic Equipment*, pp. 103-110, May 2010.

[8] J. P. C. Smeets, D. C. J. Krop, J. W. Jansen, M. A. M. Hedrix, and, E. A. Lomonova, "Optimal Design of a Pot Core Rotating Transformer," *Proceedings of the IEEE Energy Conversation Congress and Exposition*, pp. 4390-4397, Sept. 2010.

[9] A. Abdolkhani, and A. P. Hu, "A Novel Detached Magnetic Coupling Structure for Contactless Power Transfer," *Proceedings of the 37th Annual Conference of the IEEE Industrial Electronics Society*, pp. 1103-1108, Nov. 2011.

[10] J. Mühlethaler, J. W. Kolar, and A. Ecklebe, "A Novel Approach for 3D Air Gap Reluctance Calculations," *Proceedings of the 8th International Conference on Power Electronics*, The Shilla Jeju, Korea, May 30-June 3, 2011.

[11] J. A. Ferreira, "Improved Analytical Modeling of Conductive Losses in Magnetic Components," *IEEE Transactions on Power Electronics*, vol.9, no.1, pp.127-131, Jan 1994

[12] J. Biela, "Optimierung des elektromagnetisch integrierten Serien-Parallel Resonanzkonverters mit eingeprägtem Ausgangsstrom," Ph.D. dissertation (in German), Swiss Federal Institute of Technology Zurich (ETH Zürich), 2005.

[13] K. Venkatachalam, C. R. Sullivan, T. Abdallah, H. Tacca, "Accurate Prediction of Ferrite Core Loss with Nonsinusoidal Waveforms using only Steinmetz Parameters," *Proceedings of the IEEE Workshop on Computers in Power Electronics*, pp. 36- 41, 3-4 June 2002.

[14] S. P. Timoshenko and, J. N. Goodier, "Theory of Elasticity," McGraw-Hill, Kogakusha 1970.

[15] R. Gasch, R. Nordmann and, H. Pfützner, "Rotordynamik," Springer, Berlin 2001.